Evidence for self-healing benign grain boundaries and a highly defective Sb_2Se_3-CdS interfacial layer in Sb_2Se_3 thin-film photovoltaics

*Rhys E. Williams, Quentin M. Ramasse, Keith P. McKenna, Laurie J. Phillips, Peter J. Yates, Oliver S. Hutter, Ken Durose, Jonathan D. Major, Budhika G. Mendis**

R.E. Williams, Dr B.G. Mendis
Dept. of Physics, Durham University, South Road, Durham, DH1 3LE, UK
E-mail: b.g.mendis@durham.ac.uk

Prof Q.M. Ramasse
SuperSTEM, SciTech Daresbury Campus, Daresbury, WA4 4AD, UK
School of Chemical and Process Engineering, University of Leeds, Leeds, LS2 9JT, UK

Prof K.P. McKenna
Dept of Physics, University of York, Heslington, York, YO10 5DD, UK

Dr. L.J. Phillips, Dr. P.J. Yates, Dr. O.S. Hutter, Prof. K. Durose, Dr J.D. Major
Stephenson Institute for Renewable Energy, Dept of Physics, University of Liverpool, Liverpool, L69 7ZF, UK

Dr O.S. Hutter
Department of Mathematics, Physics and Electrical Engineering, Northumbria University, Newcastle upon Tyne, UK.

Abstract

The crystal structure of Sb_2Se_3 gives rise to unique properties that cannot otherwise be achieved with conventional thin-film photovoltaic materials, such as CdTe or $Cu(In,Ga)Se_2$. It has previously been asserted that, grain boundaries can be made benign provided only the weak van der Waals forces between the $(Sb_4Se_6)_n$ ribbons are disrupted. Here it is shown that non-radiative recombination is suppressed even for grain boundaries cutting across the $(Sb_4Se_6)_n$ ribbons. This is due to a remarkable self-healing process whereby atoms at the grain boundary can relax to remove any electronic defect states within the band gap. Grain boundaries can however impede charge transport due to the fact that carriers have a higher mobility along the $(Sb_4Se_6)_n$ ribbons. Because of the ribbon misorientation certain grain boundaries can effectively block charge collection. Furthermore, it is shown that CdS is not a suitable emitter to partner Sb_2Se_3 due to Sb and Se inter-diffusion. As a result a highly

defective Sb_2Se_3 interfacial layer is formed that potentially reduces device efficiency through interface recombination.

Keywords: Sb_2Se_3 photovoltaics, grain texture, Kirkendall voids, grain boundary relaxation, Sb_2Se_3-CdS interface.

1. Introduction

Traditional thin-film photovoltaics, such as CdTe and $Cu(In,Ga)Se_2$ (CIGS), are limited by grain boundaries that act as non-radiative recombination sites [1-4]. This can be linked to the crystal structure of these adamantine-based compounds, where termination of the periodic, 3D atomic bonding at the grain boundary plane gives rise to deep band gap states associated with dangling bonds. To circumvent this problem Tang and co-workers [5] proposed the use of absorber materials consisting of covalently bonded 'structural units' in the form of ribbons or layers that are held together by van der Waals forces. Provided the structural units lie parallel to the grain boundary plane only the weak van der Waals forces are disrupted; since there are no dangling bonds the grain boundary is assumed to be electrically passive. There are many semiconductor compounds that satisfy the dual requirements of ideal optical properties (i.e. Shockley-Queisser band gap and high absorption coefficient) and mixed covalent-van der Waals crystal structure that are potential new absorber materials for thin-film photovoltaics. For example, devices based on SnS[6], BiSI[7] and Sb_2Se_3[5, 8-13] have been reported in the literature. Of these Sb_2Se_3, with ribbon-shaped structural units, has shown much promise by achieving record cell efficiencies of 7.6% for planar configurations[11] and 9.2% for core-shell nanorod assemblies[13] in only a few years.

Despite the rapid increase in efficiency there is still no clear evidence to support the claim that Sb_2Se_3 grain boundaries in real thin-film devices are in fact benign. High performance Sb_2Se_3 devices consist of (211) and/or (221) oriented columnar grains[5,8-12] (here the *Pbnm* space group classification is adopted[14], where the $(Sb_4Se_6)_n$ ribbons are parallel to the crystal *c*-axis). For this grain texture the $(Sb_4Se_6)_n$ ribbons are at an angle of 37° (211) and 44° (221) from the film thickness direction, so that a high density of dangling bonds are expected at the grain boundaries. Furthermore, the carrier mobility in Sb_2Se_3 is highly anisotropic, with the [001] ribbon axis being the preferred direction for charge transport [15]. The crystallographic misorientation between two grains means that grain boundaries can be barriers to photocurrent extraction. Understanding the precise nature of the inter-granular charge transport and recombination requires uncovering the atomic scale structure of grain boundaries in Sb_2Se_3 thin-film devices.

Another interesting feature is the high defect density at the interface between Sb_2Se_3 absorber and CdS emitter layer. The interfacial defect density, measured using capacitance techniques, is in the range 10^{10}-10^{12} cm^{-2} [11,13]. Such a large interfacial defect density could be due to lattice mismatch and/or chemical inter-diffusion. The difference in crystal structures for CdS (hexagonal) and Sb_2Se_3 (orthorhombic) suggests that significant lattice mismatch must be present at the Sb_2Se_3-CdS interface. In certain cases, most notably CdTe thin-film photovoltaics [16], chemical inter-diffusion can lower the local lattice mismatch and thus the interfacial defect density as well. Several different diffusion mechanisms have been reported in the literature for Sb_2Se_3-CdS devices, such as Cd [11,17], Sb [13] and Se [12] inter-diffusion. It is important to understand the precise role of inter-diffusion on lattice mismatch and therefore the interfacial defect density, so that strategies to further improve Sb_2Se_3 device efficiencies may be proposed.

In this study aberration corrected- scanning transmission electron microscopy (AC-STEM) coupled with density functional theory (DFT) is used to characterize the structural and electronic properties of Sb_2Se_3 grain boundaries. It is shown that significant structural relaxation can take place at the grain boundaries, thereby removing any band gap states due to dangling bonds. The self-healing nature of Sb_2Se_3 suggests that grain boundary recombination may not be as harmful as previously thought. At the same time evidence is found for an unfavourable ribbon orientation giving rise to photocurrent blocking at grain boundaries. Inter-granular charge transport, rather than non-radiative recombination, therefore appears to be the device limiting factor for Sb_2Se_3 grain boundaries. Furthermore, AC-STEM analysis of the Sb_2Se_3-CdS interface shows that inter-diffusion of Sb and Se into the CdS layer causes break down of the Sb_2Se_3 crystal structure over a few nanometer thick region. Highly defective Sb_2Se_3 has band tail states that increase the interfacial defect density, potentially giving rise to lower efficiency. For higher deposition temperatures the accelerated inter-diffusion gives rise to significant Kirkendall voiding[18] at the interface. Inter-diffusion is therefore an important limitation governing the performance of Sb_2Se_3-CdS devices. Alternative emitter layers that suppress inter-diffusion, such as TiO_2 [12] and ZnO [19], are required to achieve a device free of interfacial defects.

2. Results and Discussion

2.1 Grain morphology and texture

The Sb_2Se_3-CdS and Sb_2Se_3-TiO_2 device architectures are illustrated schematically in Figures 1a and 1b respectively. Device fabrication is outlined in the Experimental Methods Section.

Sb_2Se_3-CdS devices where the Sb_2Se_3 is grown using close space sublimation (CSS) and thermal evaporation (TE) methods are examined; these growth techniques are capable of fast thin-film deposition rates and are therefore suitable for industrial scale up. Furthermore, we also examine a Sb_2Se_3-TiO_2 device grown using a two-stage CSS process [9]. This involves CSS depositing a Sb_2Se_3 seed layer prior to film growth, resulting in a more uniform thin-film with larger grain size [9]. The current density (*J*)-voltage (*V*) curves for these devices are shown in Figure 1c and the electrical properties are summarized in Table 1. The Sb_2Se_3-TiO_2 device had the highest efficiency at 6.18%, while the performance of the Sb_2Se_3-CdS devices were inferior (i.e. 2.85% for the TE device and 1.44% for CSS).

Figure 2 shows plan-view scanning electron microscopy (SEM) images of the grain structure for the different Sb_2Se_3 absorber layers, namely the CSS Sb_2Se_3-CdS device (Figure 2a), TE Sb_2Se_3-CdS device (Figure 2b), CSS Sb_2Se_3 seed layer on TiO_2 (Figure 2c) and two-stage CSS Sb_2Se_3-TiO_2 device (Figure 2d). For Sb_2Se_3 grown on CdS the CSS method produces larger grains compared to TE deposition due to the higher growth temperature and use of a N_2 inert gas atmosphere[1]. The grain coverage in CSS is sufficiently uniform to produce a continuous film, although small pin holes are still visible, especially at the grain boundary triple points. However, cross-sectional imaging using focused ion-beam (FIB) microscopy revealed that these pin holes did not extend through the entire film thickness, but rather had the effect of increasing the surface roughness, in some cases quite dramatically (see Supporting Information (i)). For Sb_2Se_3 deposited on TiO_2 using the two-stage CSS process the grain size of the seed layer (Figure 2c) is significantly smaller than the complete thin-film (Figure 2d) indicating a lack of correlation between the two microstructures.

Figure 3 shows cross-sectional scanning transmission electron microscopy (STEM) images of the devices, with the individual layers and Sb_2Se_3 grain boundaries being clearly resolved. The CSS Sb_2Se_3-CdS device (Figure 3a) has large voids that extend through almost the entire length of the Sb_2Se_3-CdS interface. Although STEM can only image a small region the same interfacial voiding was observed in FIB cross-sectional images taken from random areas of the sample (see Supporting Information (i)), indicating that it is a more general phenomenon for this device. It is due to chemical inter-diffusion at the Sb_2Se_3-CdS interface giving rise to Kirkendall voids [19] (see section 2.3 for more details). The interface voids lead to a significant drop in short circuit current density for the device (Table 1). The TE deposited Sb_2Se_3 layer shows small voids within the grain interiors as well as at the Sb_2Se_3-CdS interface (Figure 3b) but not to the same extent as the CSS sample. Incomplete densification of the Sb_2Se_3 film during low temperature TE growth is thought to give rise to the voiding within the grain interiors. These voids will lower device efficiency through reduced light absorption and by increased series resistance of the Sb_2Se_3 absorber layer.

The Sb_2Se_3 grain structure for the two-stage CSS Sb_2Se_3-TiO_2 device (Figure 3d) does not show any evidence of the starting seed layer (Figure 3c), indicating significant grain re-structuring during film growth. Electron diffraction combined with imaging in a TEM can be used to determine the [001] ribbon orientation of individual Sb_2Se_3 grains relative to the substrate (see Supporting Information (ii) for more details). In Figure 4a the ribbon orientation is plotted as a function of grain 'height', i.e. the grain dimension measured along the film thickness direction, for the two-stage CSS Sb_2Se_3-TiO_2 device. A 0^o orientation corresponds to ribbons oriented normal to the substrate and is the preferred grain texture. There is a clear correlation between grain height and orientation, such that the taller, more columnar grains also have more favorable orientations. On the other hand the equivalent

grain orientation plot for the CSS Sb_2Se_3-CdS device (Figure 4b) shows no strong correlation between grain height and orientation. X-ray diffraction showed that both the two-stage CSS Sb_2Se_3-TiO_2 and CSS Sb_2Se_3-CdS devices had a predominantly (211)/(221) texture, with the (002) peak being slightly stronger in the former (see Supporting Information (iii)). Figure 4a indicates that [001] is a fast crystal growth direction and leads to more columnar grains, although overall the film tends to adopt a (211)/(221) texture, presumably due to surface energy minimization. Fast grain growth along [001] is not however observed in the CSS Sb_2Se_3-CdS sample (Figure 4b). This is likely to be due to the opposing effect inter-diffusion of the Sb_2Se_3 layer at the Sb_2Se_3-CdS interface has on grain growth (see Figure 3a and section 2.3).

2.2. Grain boundary structural relaxation

Atomically resolved AC-STEM bright field (BF) and high angle annular dark field (HAADF) images of an individual grain boundary in the CSS Sb_2Se_3-CdS device are shown in Figure 5a and Figure 5b respectively. The grain boundary is located close to the Sb_2Se_3 film free surface, with the protective carbon layer used for TEM sample preparation visible in the top region of each micrograph (note that the FIB TEM lamella was extracted from an area outside the metal back contact). A Fourier filtered HAADF image, shown in Figure 5c, provides a clearer view of the boundary structure. Using Fourier transforms and the atomic structure of the HAADF image the orientation of the grain to the left of the grain boundary was found to be [100], while the right hand grain is close to a $[\mathbf{2\bar{1}1}]$ orientation. The projected direction of the [001] oriented ribbons within each grain is annotated in Figure 5c, with the ribbons for the left grain being in-plane. For hole collection at the metal back contact the overall direction of hole transport must be in the vertical direction with respect to the AC-

STEM images in Figure 5a-5c. The mobility is however highest along the [001] ribbon direction [15]. The orientation of the ribbons either side of the grain boundary means that on crossing the grain boundary holes cannot reach the back contact unless some amount of inter-ribbon charge hopping takes place. Inter-ribbon charge hopping is much less efficient compared to transport along the ribbon, so that in this particular case the grain boundary impedes collection of the hole current. This phenomenon is due entirely to the anisotropy of the Sb_2Se_3 crystal structure, and therefore similar considerations apply to grain boundaries and electron transport towards the space charge region.

The grain boundary plane in the AC-STEM images is indexed as (041) and (273) in the crystal coordinates of the left and right hand grains respectively. Figure 5d is an enlarged view of the grain boundary region extracted from the filtered HAADF image (Figure 5c). The grain boundary plane is not atomistically flat and contains several (001) steps. Simulating the full grain boundary using DFT is computationally demanding since the absence of simple periodic boundary conditions requires an extremely large supercell. As a compromise DFT calculations are performed on (001) and (041), (273) free surfaces, which are taken to represent the grain boundary steps and average grain boundary plane respectively. It is not possible to accurately represent a grain boundary by a free surface when there is coupling between atoms on either side of the boundary. In Sb_2Se_3 though the strong covalent bonding is confined to the [001] ribbons, and for the grain boundary in Figure 5c the ribbon orientation changes by 74^o on crossing the grain boundary plane (here the out-of-plane component of the ribbon direction in the right hand grain has been taken into account). Since the ribbon directions are close to orthogonal the coupling is likely to be weak, thus justifying the use of free surfaces in the simulation.

Supercells of single crystal Sb_2Se_3 were constructed to determine the electronic density of states (DOS) at the free surface and the bulk of the crystal respectively. The free surface DOS was calculated before and after atom relaxation using the HSE06 hybrid functional together with the D3 Grimme dispersion correction to describe the Van der Waals interactions between the $(Sb_4Se_6)_n$ ribbons (HSE+D3) [20]. The band gap and lattice constants of Sb_2Se_3 can be accurately predicted and the pseudopotential has also been previously used in Sb_2Se_3 defect calculations [21]. Figure 6a shows the supercell for the (001) free surface viewed end-on along the [100] direction. The bulk and surface DOS were extracted from atoms within the box regions in Figure 6a and are shown superimposed in Figure 6b. As expected there are no electronic states within the band gap for the 'perfect' bulk crystal. The unrelaxed (001) free surface has electronic states that are close to the middle of the band gap and are therefore potential non-radiative recombination defect levels [22]. These deep defect states are due to dangling bonds at the free surface. Shallower donor states are also present but are comparatively benign to device performance. Surprisingly structural relaxation completely eliminates all defect states within the band gap, even though many of the broken bonds still remain. In fact structural relaxation is so strong that the coordination of some of the sub-surface atoms are also altered as a result. Furthermore, there is no shift in the valence band maximum or conduction band minimum at the relaxed free surface compared to the bulk. This means that there is no energetic barrier to electron or hole transport, unlike, for example, grain boundaries in $CuInSe_2$ which are thought to be hole barriers due to a valence band offset between grain boundary and grain interior [3]. Similar trends are also observed for the (041) free surface (Figure 6c,d**)**. The supercell for a (273) free surface has too many atoms to simulate using HSE06+D3, and therefore a computationally faster, but less accurate, PBE functional was used for optimization. Even here it was found that deep defect states were removed after surface relaxation (see Supporting Information (iv)). This was also true for a

(041) symmetric tilt boundary simulated using the HSE06 functional (see Supporting Information (iv)). These results suggest that the covalent bonding in $(Sb_4Se_6)_n$ ribbons can accommodate large amounts of strain, allowing for significant self-healing of the grain boundary and removal of electronic defect states. This contradicts the commonly held view that only grain boundaries that disrupt the weak van der Waals bonding in Sb_2Se_3 are benign. In fact anisotropic charge transport across the grain boundary appears to have a more important effect on device performance than grain boundary recombination.

2.3. Inter-diffusion at the Sb_2Se_3-CdS interface

In photovoltaic heterojunctions, chemical stability of the partner materials is crucial for the proper working of the device. In this section it will be shown that the Sb_2Se_3-CdS interface is highly unstable, leading to a structural breakdown of the Sb_2Se_3 layer and in extreme cases the formation of interfacial voids. First consider the CSS Sb_2Se_3-CdS device with the Sb_2Se_3-CdS interfacial voids (Figure 3a). The distribution of chemical elements around the Sb_2Se_3-CdS interface region was mapped using energy dispersive X-ray (EDX) spectroscopy in the STEM. The region selected for chemical mapping had clear interfacial voiding and the results are shown in Figure 7. Se and Sb are both present in the CdS layer with the latter having a higher concentration towards the CdS-ZnO high resistive layer interface. The observation of residual Sb signal in the fluorine doped SnO_2 (FTO) transparent conducting oxide layer (Figure 7c) is a data processing artefact arising from the overlap of the Sn and Sb L-characteristic X-ray peaks. There is no evidence for appreciable Cd or S in the Sb_2Se_3 layer, implying faster diffusion kinetics from Sb_2Se_3 into CdS compared to diffusion in the opposite direction. Similar trends were also observed in regions where the Sb_2Se_3-CdS interface remained intact, such as the circled area in Figure 3a (see Supporting Information (v)). For

vacancy assisted diffusion mechanisms an asymmetry in the diffusion rate across a junction creates pores, known as Kirkendall voids [18], that form on the side that has the larger diffusion flux, which in this case is Sb_2Se_3. This is likely to be the origin of the Sb_2Se_3-CdS interfacial voiding. For example, in samples where the inter-diffusion is suppressed, either through a lower Sb_2Se_3 deposition temperature or by using an inert emitter layer such as TiO_2, extensive interfacial voiding is not present (see below). Furthermore, it is unlikely the interfacial voids could have arisen through film delamination, since the network of interfacial voids in Figure 3a has a convoluted geometry that resembles the grain structure of the Sb_2Se_3 film, which is unlike interfacial delamination where a more planar breakage is expected.

Figure 7i is an EDX linescan of the elements across the CSS Sb_2Se_3-CdS interface. The results were acquired along the line annotated in Figure 7a and the maximum EDX signal for each element was normalized for visual clarity. The relative Se concentration within the CdS layer is highest towards the Sb_2Se_3 side. A clear separation of Se and S profiles is visible in this region and suggests that the local Se concentration may be sufficiently high to form a separate CdSe layer alongside the Cd(S,Se) inter-diffused region. Further evidence for this is obtained by noting that the Cd map (Figure 7d) appears thicker than the S map (Figure 7e). Formation of CdSe or Cd(S,Se) is not unexpected [12] since it has the same crystal structure (i.e. wurtzite) as CdS and furthermore Se has a high solubility in CdS [23]. In Figure 7i the inter-diffused Sb has the highest concentration in approximately the same region as S, which could suggest the formation of a Sb_2S_3 layer at the CdS-ZnO interface. However, there is no direct correlation between the Sb (Figure 7c) and S (Figure 7e) maps which eliminates this possibility. The fact that the Sb is concentrated towards the ZnO interface suggests that it is not very soluble in Cd(S,Se).

EDX maps and linescans were also acquired from the TE Sb_2Se_3-CdS device. This sample had a lower Sb_2Se_3 deposition temperature and only minor interface voids (Figure 3b). The EDX results (see Supporting Information (vi)) did not show any evidence for inter-diffusion to within the measurement sensitivity and spatial resolution of the microscope, which was a non-corrected, field emission gun transmission electron microscope (FEG TEM). AC-STEM can however produce atomic sized beams [24] and therefore has a higher resolution and sensitivity. Figure 8a shows a medium angle annular dark field (MAADF) image of the TE Sb_2Se_3-CdS interface acquired using an AC-STEM microscope. The Sb_2Se_3 region in the image consists of a single grain in the $[\bar{1}10]$ orientation. The lattice structure of the CdS region is also visible. In between these two crystalline layers there is a ~8 nm thick region with no resolved atomic structure, labelled 'intermediate layer'. The distribution of Sb and Cd over the entire region in Figure 8a was mapped using electron energy loss spectroscopy (EELS) spectrum imaging [25]. From the area maps line profiles for Sb and Cd were obtained by integrating the EELS signal in the horizontal direction, i.e. parallel to the Sb_2Se_3-CdS interface, and are shown superimposed in Figure 8b. There is a peak in the Sb signal (vertical arrow) at the interface between the 'intermediate layer' and CdS; the location of this peak is indicated by the horizontal white line in Figure 8a. The 'intermediate layer' contains Sb but not Cd, indicating that it was initially part of the $[\bar{1}10]$-oriented Sb_2Se_3 grain. The absence of $[\bar{1}10]$ atomic resolution contrast in the 'intermediate layer' implies that the crystal structure has broken down due to diffusion of Sb (and possibly Se) towards CdS.

Although the lower deposition temperature of the thermal evaporation process had largely eliminated Kirkendall voiding there is still some diffusion that takes place, giving rise to a highly defective Sb_2Se_3 intermediate layer few nanometers in thickness. This is consistent with previous electrical measurements [11,13] that reported a high interfacial defect density for

Sb_2Se_3-CdS devices. The defective Sb_2Se_3 layer can result in higher rates of interfacial recombination, thereby reducing device efficiency. Our results demonstrate that CdS is not a suitable emitter layer for Sb_2Se_3, since even under favorable conditions the inter-diffusion is unlikely to be fully suppressed at the atomic scale. Empirically it has been shown that device performance can be improved by using TiO_2 as either a barrier layer [13] or to fully replace CdS as the emitter layer [12]. EDX maps and linescans (Figure 9) have been acquired from the CSS Sb_2Se_3-TiO_2 device using a non-corrected FEG TEM and show no evidence for inter-diffusion to within the sensitivity and resolution of the technique. For example, the Sb and Se line profiles (Figure 9g) show strong overlap at the Sb_2Se_3-TiO_2 interface (the subsequent increase in Sb signal is a processing artefact due to overlap of the Sb and Sn X-ray peaks from the FTO layer). The lack of any observable inter-diffusion is consistent with the higher reported efficiencies of Sb_2Se_3-TiO_2 devices (see also Table 1), although higher resolution AC-STEM measurements are required to confirm that the interface region remains defect free even at the atomic scale. Another strategy to reduce the deleterious effects of interfacial recombination is to use multiple emitter layers with systematic conduction band offsets, so that a cascading energy landscape is created for electron transport, such as in, for example, a double TiO_2/CdS emitter paired with mixed anion $Sb_2(S,Se)_3$ absorber layer [26-28].

3. Conclusions

A combined electron microscopy and DFT study has revealed several unexpected properties about Sb_2Se_3 thin-film photovoltaic devices. The first is the self-healing property of Sb_2Se_3 grain boundaries, where electronic states deep within the band gap due to dangling bonds are removed by grain boundary atom relaxation. The assumption of rapid recombination at grain boundaries where the covalent bonding along the $(Sb_4Se_6)_n$ ribbons is disrupted must

therefore be revised. However, grain boundaries can still influence device performance through anisotropic charge transport which occurs predominantly along the $(Sb_4Se_6)_n$ ribbons. Misorientation of the ribbons either side of the boundary means that certain grain boundaries impede charge transport to either the space charge region (electrons) or back contact (holes). The ideal film texture therefore consists of (001) oriented grains. [001] is shown to be a fast crystal growth direction and results in columnar grains, although in practice most Sb_2Se_3 thin-films are found to have a (211)/(221) texture. Strategies to promote (001) grain texture are therefore a direct route to optimizing device efficiency. It has also been demonstrated that CdS is not a suitable emitter material due to rapid inter-diffusion of Sb and Se from Sb_2Se_3. Even when the diffusion is largely suppressed, such as by lowering the deposition temperature, a highly defective interfacial layer of Sb_2Se_3 can form on the atomic scale. The increased interfacial recombination results in lower device efficiencies. Achieving high efficiencies would therefore require a diffusion barrier layer between the CdS and Sb_2Se_3 or the use of alternative, chemically inert emitter layers.

4. Experimental Method

Device fabrication: For the CSS Sb_2Se_3-CdS device a high resistive ZnO layer was used in between the FTO and CdS so that a thinner CdS layer could be deposited, which has the effect of reducing parasitic absorption of high energy photons. Both ZnO and CdS were deposited by sputtering. The conditions were 150 W power for 50 minutes at room temperature (ZnO) and 60 W for 15 minutes at 200^{o}C (CdS). CSS deposition of Sb_2Se_3 took place for 15 minutes with a source temperature of 460^o under 13 mbar N_2 atmosphere. In order to halt film deposition the pressure was increased to 400 mbar and the heating switched off. The TE Sb_2Se_3-CdS samples were deposited on sputtered CdS (with no underlying ZnO layer) with the unheated substrate under vacuum ($5x10^{-5}$ mbar) and a source-substrate

distance of 20 cm. The resulting absorber layer was of poor quality and therefore had to be hot plate annealed under N_2 atmosphere in a glove box at 350^{o}C for 30 minutes. For the two-stage CSS Sb_2Se_3-TiO_2 device the TiO_2 was spin coated at 3000 rpm for 30 s using a 0.15 M and 0.30 M titanium isopropoxide in ethanol solution with drying at 120^{o}C for 10 minutes in N_2 after each deposition. The TiO_2 was then sintered in air at 500^{o}C for 30 minutes. The two-stage CSS growth first involved depositing a Sb_2Se_3 seed layer with source and substrate temperatures of 340^o and 390^{o}C respectively under 0.05 mbar N_2 for 2 minutes. The seed layer was annealed for 10 minutes with the N_2 pressure increased to 260 mbar. The second stage of Sb_2Se_3 deposition took place for 15 minutes under 13 mbar N_2 pressure with the source temperature increased to 460^{o}C. All devices were grown on NSG TEC10 glass. Further details can be found in references (9), (12) and (29-30).

Electron Microscopy: TEM cross-section samples were prepared using an FEI Helios 600 Nanolab dual-beam FIB [(31)]. The Sb_2Se_3 layer back surface was carbon coated to minimize charging followed by platinum layer deposition to prevent gallium ion-beam damage during milling. A 2 kV ion-beam voltage was used for the final thinning of the TEM lamellae. The FIB was also used to acquire plan-view and cross-sectional SEM images at 3 kV electron beam voltage. TEM/STEM characterisation was carried out in a JEOL 2100F FEG TEM operating at 200 kV and Oxford Instruments X-Max 65T silicon drift detector for EDX analysis. High resolution AC-STEM analysis was carried out in a Nion UltraSTEM 100 MC Hermes Microscope at the SuperSTEM facility, Daresbury UK. The operating voltage was 60 kV and the STEM probe convergence semi-angle was 31 mrad. The detector inner and outer angles were 55, 82 mrad for MAADF imaging and 82,180 mrad for HAADF imaging. EELS spectra were acquired on a Gatan Enfinium spectrometer with 0.2 eV/channel dispersion and 44 mrad spectrometer collection semi-angle. Standard power law fitting[(32)] was used to subtract the background from core loss edges.

DFT simulations: Spin polarized density functional theory calculations were carried out using the projector augmented wave method and a plane wave basis as implemented in the Vienna Ab initio Simulation Package (VASP) [33-34]. We employ the HSE06 hybrid functional together with the D3 Grimme dispersion correction to describe the Van der Waals interactions between the $(Sb_4Se_6)_n$ ribbons (HSE+D3) [20, 35]. The bulk crystal was optimized using a 350 eV plane wave cut off and a 2x2x6 gamma-centered k-point grid for Brillouin zone sampling, yielding lattice constants of a = 11.52 Å, b = 11.91 Å and c =3.98 Å. Surface supercells were constructed based on the optimized structure at the HSE+D3 level and including a vacuum gap of at least 10 Å. For the (001) and (041) surface we sample the Brillouin zone with a 1x3x3 k-point grid and for the (273) we employ a 1x2x1 k-point grid. The Hartree-Fock kernel is sampled at the gamma point only in the surface calculations. The (001) and (410) surface supercells are optimized at the HSE+D3 level until all forces are less than 0.05 eV/Å. The (273) surface supercell is instead optimized using the PBE exchange correlation functional however keeping the supercell dimensions corresponding to the HSE+D3 optimized bulk until cell. All surface structures were visualized using the VESTA code [36].

5. Supporting Information

Includes (i) FIB cross-sectional images of devices, (ii) Measuring the orientation of Sb_2Se_3 ribbons relative to the substrate, (iii) X-ray diffraction plots, (iv) Electronic Density of States (DOS) for the (273) free surface and (041) tilt boundary, (v) EDX chemical mapping across an intact CSS Sb_2Se_3-CdS interface, and (vi) EDX chemical mapping across the TE Sb_2Se_3-CdS interface.

6. Acknowledgements

Instrument time at the EPSRC National Research Facility for Advanced Electron Microscopy, SuperSTEM, is gratefully acknowledged. BGM would like to thank the North East Centre for Energy Materials (NECEM) for funding (EPSRC grant EP/R021503/1). KPM acknowledges support from the EPSRC (EP/P023843/1). This work made use of the facilities of Archer, the UK's national high-performance computing service, via our membership in the UK HPC Materials Chemistry Consortium, which is funded by the EPSRC (EP/L000202, EP/R029431) and the Viking Cluster, which is a high‐performance computer facility provided by the University of York. All data relating to the density functional theory calculations created during this research are available on request from the University of York Research database (https://doi.org/TBC).

7. References

(1) Major, J.D.; Proskuryakov, Y.Y.; Durose, K.; Zoppi, G.; Forbes, I. Control of Grain Size in Sublimation-Grown CdTe, and the Improvement in Performance of Devices with Systematically Increased Grain Size *Sol. Energy Mat. Sol. Cells* 2010, 94, 1107-1112.

(2) Mendis, B.G.; Gachet, D.; Major, J.D.; Durose, K. Long Lifetime Hole Traps at Grain Boundaries in CdTe Thin-Film Photovoltaics *Phys. Rev. Lett.* 2015, 115, 218701 (5 pages).

(3) Persson, C.; Zunger, A. Anomalous Grain Boundary Physics in Polycrystalline $CuInSe_2$: The Existence of a Hole Barrier *Phys. Rev. Lett.* 2003, 91, 266401 (4 pages).

(4) Abou-Ras, D.; Schaffer, B.; Schaffer, M.; Schmidt, S.S.; Caballero, R.; Unold, T. Direct Insight into Grain Boundary Reconstruction in Polycrystalline Cu(In,Ga)Se_2 with Atomic Resolution *Phys. Rev. Lett.* 2012, 108, 075502 (5 pages).

(5) Zhou, Y.; Wang, L.; Chen, S.; Qin, S.; Liu, X.; Chen, J.; Xue, D-J.; Luo, M.; Cao, Y.; Cheng, Y.; Sargent, E.H.; Tang, J. Thin-film Sb_2Se_3 Photovoltaics with Oriented One-Dimensional Ribbons and Benign Grain Boundaries *Nat. Photonics* 2015, 9, 409-416.

(6) Sinsermsuksakul, P.; Sun, L.; Lee, S.W.; Park, H.H.; Kim, S.B.; Yang, C.; Gordon, R.G. Overcoming Efficiency Limitations of SnS-Based Solar Cells *Adv. Energy Mater.* 2014, 4, 1400496 (7 pages).

(7) Tiwari, D.; Cardoso-Delgado, F.; Alibhai, D.; Mombrú, M.; Fermin, D.J. Photovoltaic Performance of Phase-Pure Orthorhombic BiSI Thin-Films *ACS Appl. Energy Mater.* 2019, 2, 3878-3885.

(8) Chen, C.; Wang, L.; Gao, L.; Nam, D.; Li, D.; Li, K.; Zhao, Y.; Ge, C.; Cheong, H.; Liu, H.; Song, H.; Tang, J. 6.5% Certified Efficiency Sb_2Se_3 Solar Cells Using PbS Colloidal Quantum Dot Film as Hole-Transporting Layer *ACS Energy Lett.* 2017, 2, 2125-2132.

(9) Hutter, O.S.; Phillips, L.J.; Durose, K.; Major, J.D. 6.6% Efficient Antimony Selenide Solar Cells Using Grain Structure Control and an Organic Contact Layer *Sol. Energy Mat. Sol. Cells* 2018, 188, 177-181.

(10) Li, D-B.; Yin, X.; Grice, C.R.; Guan, L.; Song, Z.; Wang, C.; Chen, C.; Li, K.; Cimaroli, A.J.; Awni, R.A.; Zhao, D.; Song, H.; Tang, W.; Yan, Y.; Tang, J. Stable and Efficient CdS/Sb_2Se_3 Solar Cells Prepared by Scalable Close Space Sublimation *Nano Energy* 2018, 49, 346-353.

(11) Wen, X.; Chen, C.; Lu, S.; Li, K.; Kondrotas, R.; Zhao, Y.; Chen, W.; Gao, L.; Wang, C.; Zhang, J.; Niu, G.; Tang, J. Vapor Transport Deposition of Antimony Selenide Thin Film Solar Cells With 7.6% Efficiency *Nature Comms.* 2018, 9, 2179-2189.

(12) Phillips, L.J.; Savory, C.N.; Hutter, O.S.; Yates, P.J.; Shiel, H.; Mariotti, S.; Bowen, L.; Birkett, M.; Durose, K.; Scanlon, D.O.; Major, J.D. Current Enhancement Via a TiO2 Window Layer for CSS Sb2Se3 Solar Cells: Performance Limits and High *V*oc *IEEE J. Photovoltaics* 2019, 9, 544-551.

(13) Li, Z.; Liang, X.; Li, G.; Liu, H.; Zhang, H.; Guo, J.; Chen, J.; Shen, K.; San, X.; Yu, W.; Schropp, R.E.I.; Mai, Y. 9.2%-Efficient Core-Shell Structured Antimony Selenide Nanorod Array Solar Cells *Nature Comms.* 2019, 10, 125-133.

(14) Tideswell, N.W.; Kruse, F.H.; McCullough, J.D. The Crystal Structure of Antimony Selenide, Sb_2Se_3 *Acta Crystallogr.* 1957, 10, 99-102.

(15) Chen, C.; Bobela, D.C.; Yang, Y.; Lu, S.; Zeng, K.; Ge, C.; Yang, B.; Gao, L.; Zhao, Y.; Beard, M.C.; Tang, J. Characterization of Basic Physical Properties of Sb_2Se_3 and Its Relevance for Photovoltaics *Front. Optoelectron.* 2017, 10, 18-30.

(16) Taylor, A.A.; Major, J.D.; Kartopu, G.; Lamb, D.; Duenow, J.; Dhere, R.G.; Maeder, X.; Irvine, S.J.C.; Durose, K.; Mendis, B.G. A Comparative Study of Microstructural Stability and Sulphur Diffusion in CdS/CdTe Photovoltaic Devices *Sol. Energy Mat. Sol. Cells* 2015, 141, 341-349.

(17) Zhou, Y.; Li, Y.; Luo, J.; Li, D.; Liu, X.; Chen, C.; Song, H.; Ma, J.; Xue, D-J.; Yang, B.; Tang, J. Buried Homojunction in CdS/Sb_2Se_3 Thin Film Photovoltaics Generated By Interfacial Diffusion *Appl. Phys. Lett.* 2017, 111, 013901 (5 pages).

(18) Porter, D.A.; Easterling, K.E.; Sherif, M.Y. *Phase Transformations in Metals and Alloys*, 3rd Edition, CRC Press, USA 2009.

(19) Wang, L.; Li, D-B.; Li, K.; Chen, C.; Deng, H-X.; Gao, L.; Zhao, Y.; Jiang, F.; Li, L.; Huang, F.; He, Y.; Song, H.; Niu, G.; Tang, J. Stable 6%-Efficient Sb_2Se_3 Solar Cells With a ZnO Buffer Layer *Nat. Energy* 2017, 2, 17046 (9 pages).

(20) Krukau, A.V.; Vydrov, O.A.; Izmaylov, A.F.; Scuseria, G.E. Influence of the Exchange Screening Parameter on the Performance of Screened Hybrid Functionals *J. Chem. Phys.* 2006, 125, 224106 (5 pages).

(21) Savory, C.N.; Scanlon, D.O. The Complex Defect Chemistry of Antimony Selenide *J. Mater. Chem. A* 2019, 7, 10739-10744.

(22) Landsberg, P.T. *Recombination in Semiconductors*, Cambridge University Press, Cambridge 1991.

(23) Hassanien, A.S.; Akl, A.A. Effect of Se Addition on Optical and Electrical Properties of Chalcogenide CdSSe Thin Films *Superlattice and Microstructures* 2016, 89, 153-169.

(24) Krivanek, O.L.; Ursin, J.P.; Bacon, N.J.; Corbin, G.J.; Dellby, N.; Hrncirik, P.; Murfitt, M.F.; Own, C.S.; Szilagyi, Z.S. High-Energy-Resolution Monochromator For Aberration-Corrected Scanning Transmission Electron Microscopy/Electron Energy-Loss Spectroscopy *Phil. Trans. R. Soc. A* 2009, 367, 3683-3697.

(25) Jeanguillaume, C.; Colliex, C. Spectrum-Image: The Next Step in EELS Digital Acquisition and Processing *Ultramicroscopy* 1989, 28, 252-257.

(26) Jaramillo-Quintero, O.A.; Rincón, M.E.; Vásquez-García, G.; Nair, P.K. Influence of the Electron Buffer Layer on the Photovoltaic Performance of Planar $Sb_2(S_xSe_{1-x})_3$ Solar Cells *Prog. Photo.: Res. Appl.* 2018, 26, 709-717.

(27) Wang, W.; Wang, X.; Chen, G.; Chen, B.; Cai, H.; Chen, T.; Chen, S.; Huang, Z.; Zhu, C.; Zhang, Y. Promising $Sb_2(S,Se)_3$ Solar Cells with High Open Circuit Voltage by Application of a TiO_2/CdS Double Buffer Layer *Solar RRL* 2018, 2, 1800208 (9 pages).

(28) Wang, X.; Tang, R.; Yin, Y.; Ju, H.; Li, S.; Zhu, C.; Chen, T. Interfacial Engineering for High Efficiency Solution Processed Sb_2Se_3 Solar Cells *Sol. Energy Mat. Sol. Cells* 2019, 189, 5-10.

(29) Yates, P.J. *Emerging Absorber Materials for Sustainable Photovoltaics*, PhD Thesis, University of Liverpool, UK 2018.

(30) Williams, R.E. *Microstructural Defects in Antimony Selenide Solar Cells*, MRes Thesis, Durham University, UK 2019.

(31) Schaffer, M.; Schaffer, B.; Ramasse, Q. Sample Preparation for Atomic-Resolution STEM at Low Voltages by FIB *Ultramicroscopy* 2012, 114, 62-71.

(32) Egerton, R.F. *Electron Energy Loss Spectroscopy in the Electron Microscope*, 2nd Edition, Plenum Press, New York 1996.

(33) Kresse, G.; Furthmüller, J. Efficient Iterative Schemes for *Ab Initio* Total-Energy Calculations Using a Plane-Wave Basis Set *Phys. Rev. B* 1996, 54, 11169-11186.

(34) Kresse, G.; Furthmüller, J. Efficiency of Ab-Initio Total Energy Calculations For Metals and Semiconductors Using a Plane-Wave Basis Set *Comput. Mater. Sci*. 1996, 6, 15-50.

(35) Grimme, S. Accurate Description of Van Der Waals Complexes by Density Functional Theory Including Empirical Corrections *J. Comput. Chem*. 2004, 25, 1463-1473.

(36) Momma, K.; Izumi, F. *VESTA 3* for Three-Dimensional Visualization of Crystal, Volumetric and Morphology Data *J. Appl. Crystallogr*. 2011, 44, 1272-1276.

Table 1. Sb_2Se_3 thin-film devices and their electrical properties (V_{oc} is the open circuit voltage, J_{sc} is the short circuit current density and R_s, R_{sh} are series and shunt resistances respectively). 'CSS' and 'TE' are abbreviations for close space sublimation and thermal evaporation.

Device	Efficiency (%)	V_{oc} (V)	J_{sc} (mA/cm^2)	Fill factor (%)	R_s (Ωcm^2)	R_{sh} (Ωcm^2)
CSS Sb_2Se_3- CdS	1.44	0.42	7.57	45.48	18.40	183.72
TE Sb_2Se_3- CdS	2.85	0.38	20.20	37.10	11.25	37.90
Two-stage CSS Sb_2Se_3-TiO_2	6.18	0.40	31.44	49.20	3.25	61.64

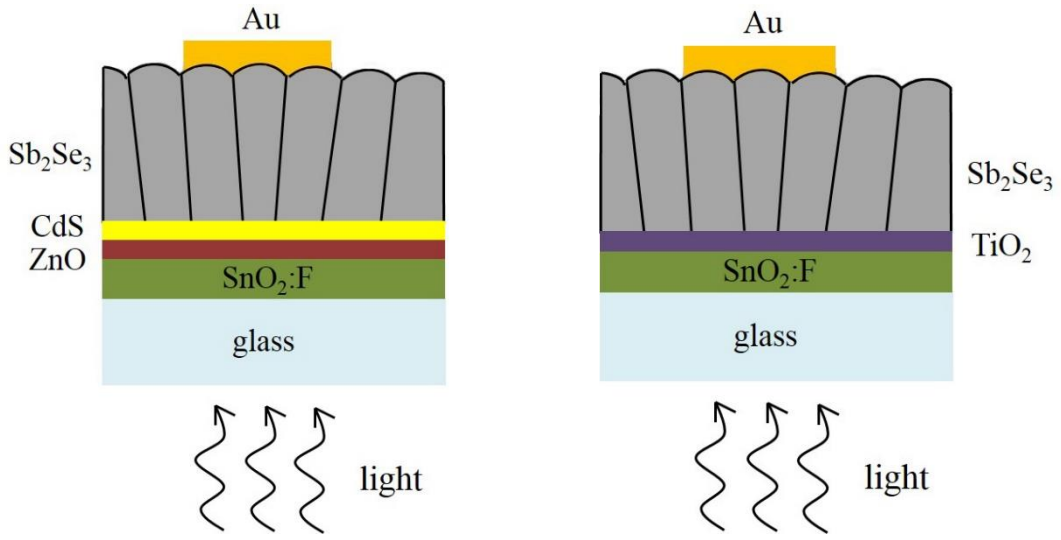

(a) **(b)**

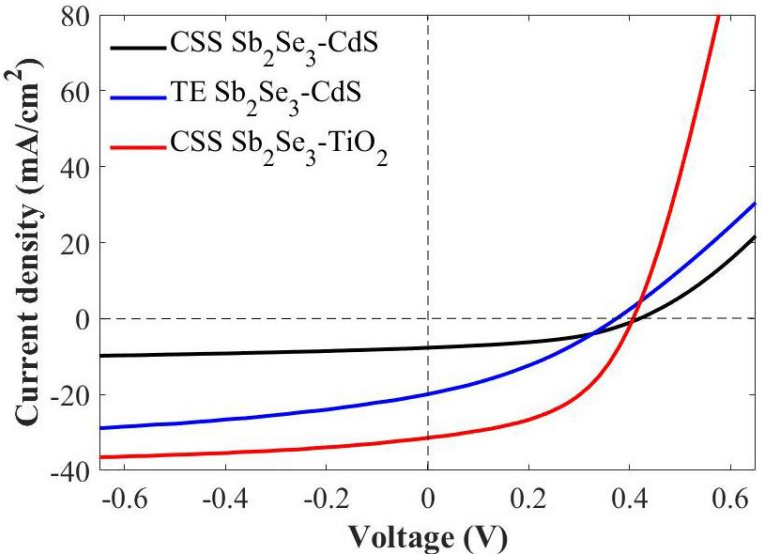

(c)

Figure 1. Schematic illustration of (a) Sb_2Se_3-CdS and (b) Sb_2Se_3-TiO_2 device structures. The individual layers are not drawn to scale. Devices are fabricated in the superstrate configuration with light entering through the glass. (c) plots *JV*-curves for the different devices. 'CSS' and 'TE' are abbreviations for close space sublimation and thermal evaporation.

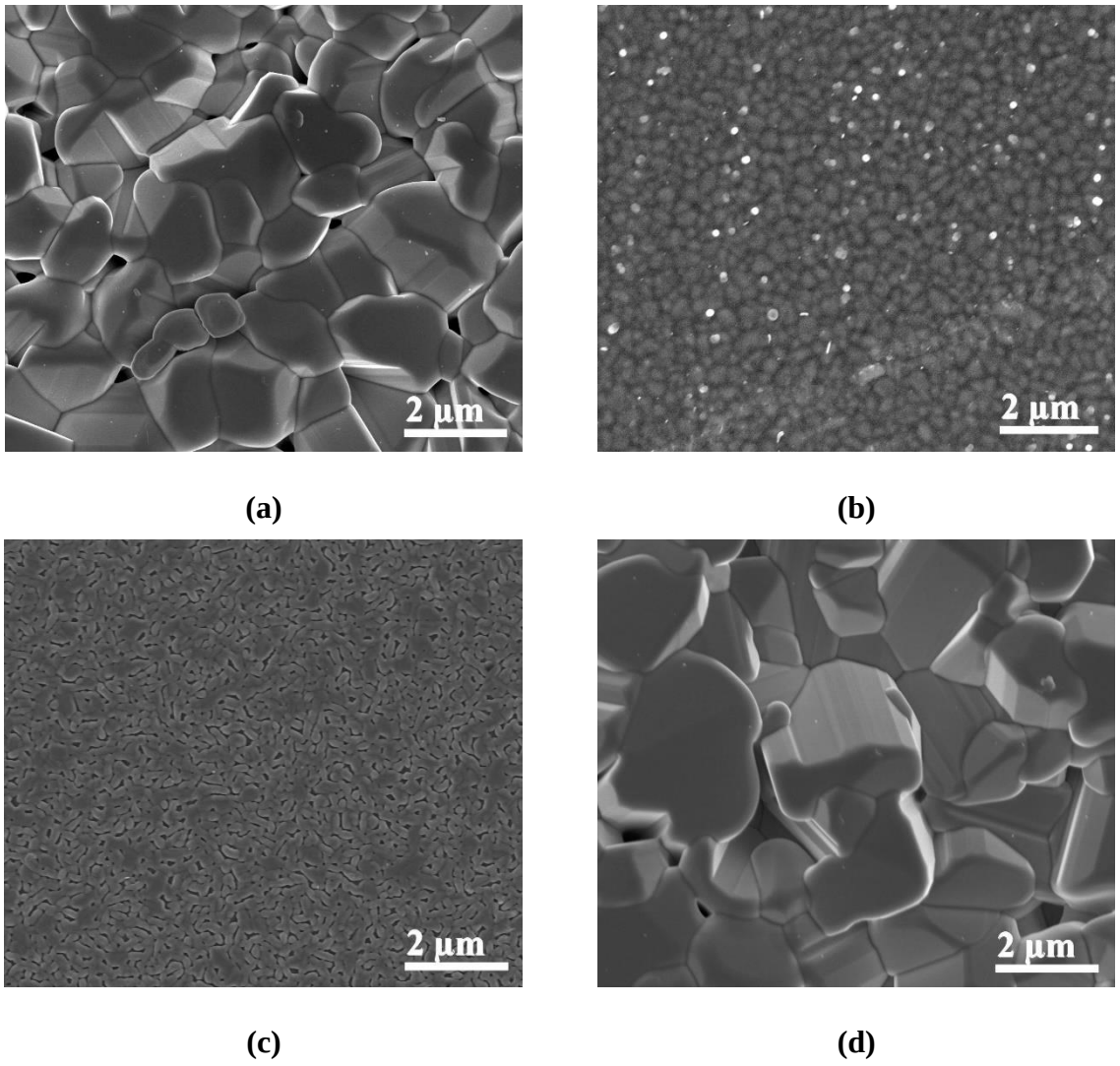

Figure 2. Secondary electron SEM images of the Sb_2Se_3 absorber layer back surface. The devices are (a) CSS Sb_2Se_3-CdS, (b) TE Sb_2Se_3-CdS, (c) seed layer CSS Sb_2Se_3-TiO_2 and (d) two-stage CSS Sb_2Se_3-TiO_2, where CSS is close space sublimation and TE is thermal evaporation.

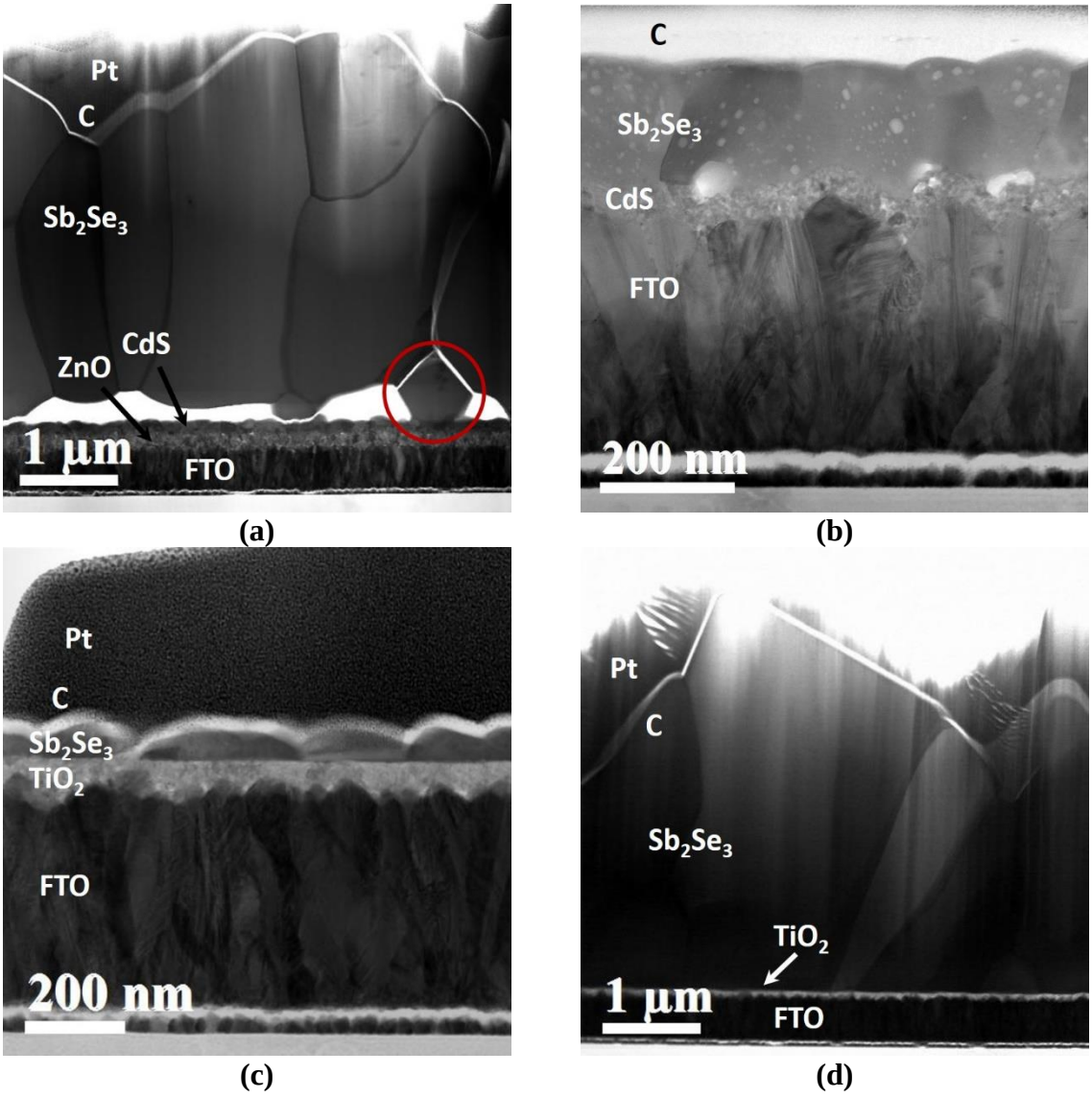

Figure 3. STEM bright field images of Sb_2Se_3 thin-film photovoltaics. The devices are (a) CSS Sb_2Se_3-CdS, (b) TE Sb_2Se_3-CdS, (c) seed layer CSS Sb_2Se_3-TiO_2 and (d) two-stage CSS Sb_2Se_3-TiO_2, where CSS is close space sublimation and TE is thermal evaporation. The carbon and platinum layers are protective layers used in FIB TEM sample preparation. Note the differences in scale between images.

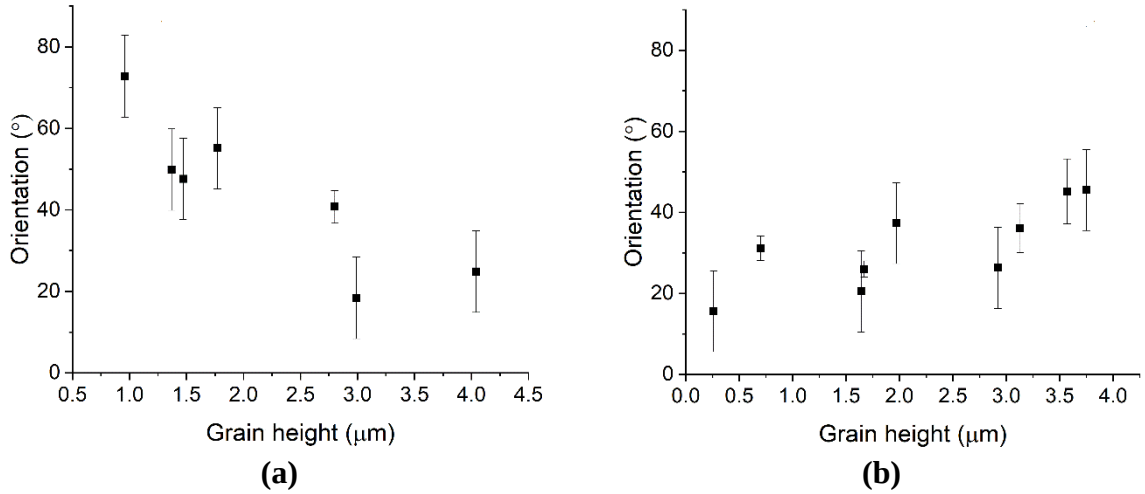

Figure 4. Orientation of $(Sb_4Se_6)_n$ ribbons plotted as a function of grain 'height', i.e. grain dimension along the Sb_2Se_3 film thickness direction. A 0^o orientation corresponds to the $(Sb_4Se_6)_n$ ribbons lying normal to the substrate. The results for the two-stage CSS Sb_2Se_3-TiO_2 device are shown in (a) while (b) corresponds to the CSS Sb_2Se_3-CdS device, where CSS is close space sublimation.

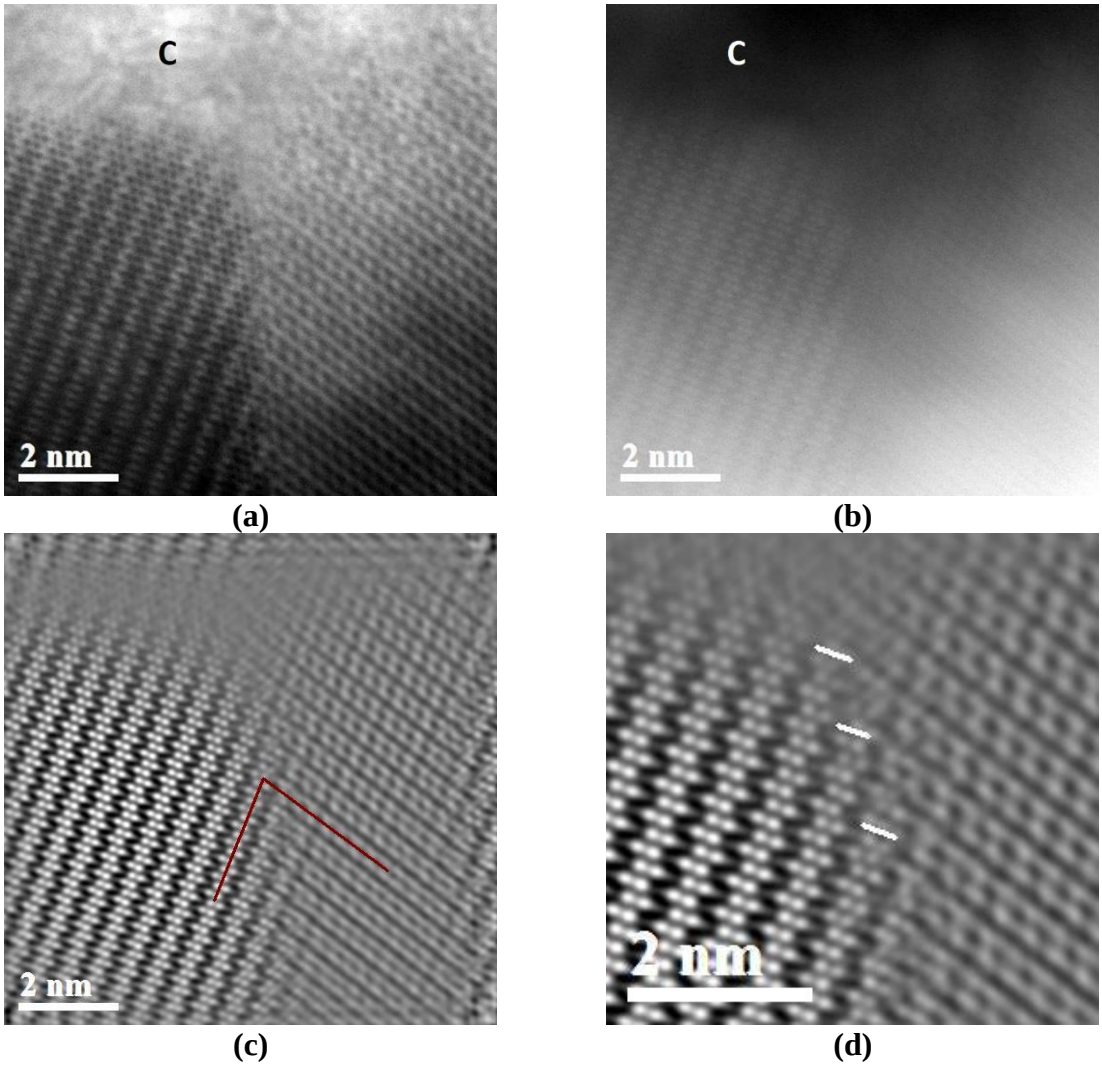

Figure 5. AC-STEM images of a Sb_2Se_3 grain boundary in the close space sublimated Sb_2Se_3-CdS device. The simultaneously acquired bright field and HAADF images are shown in (a) and (b) respectively. The carbon protective layer, used for TEM sample preparation, is annotated with the letter 'C'. The Fourier filtered image of (b) is shown in (c) with the red lines representing the projected direction of the $(Sb_4Se_6)_n$ ribbons either side of the grain boundary. (d) is an enlarged image of the grain boundary region in (c) where the presence of (001) steps is indicated by the white line segments.

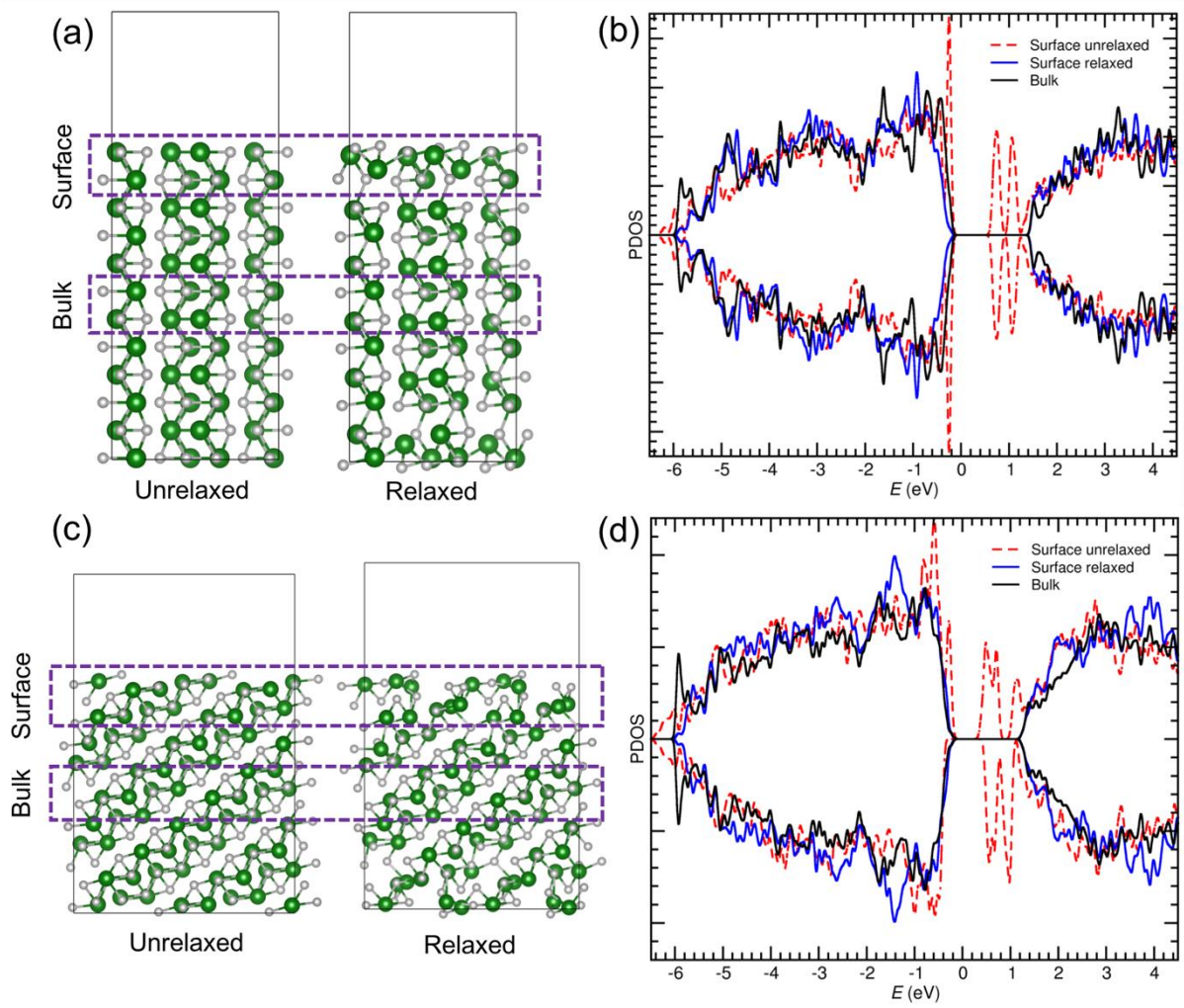

Figure 6. (a) The structure of the (001) Sb_2Se_3 free surface (shown in [100] projection) before and after geometry optimization at the HSE+D3 level. The box regions enclose the atoms used for extracting the bulk and surface DOS respectively. (b) shows superimposed spin polarized DOS plots for the (001) free surface (before and after relaxation) and the bulk. (c) and (d) show the same information for (041) free surface.

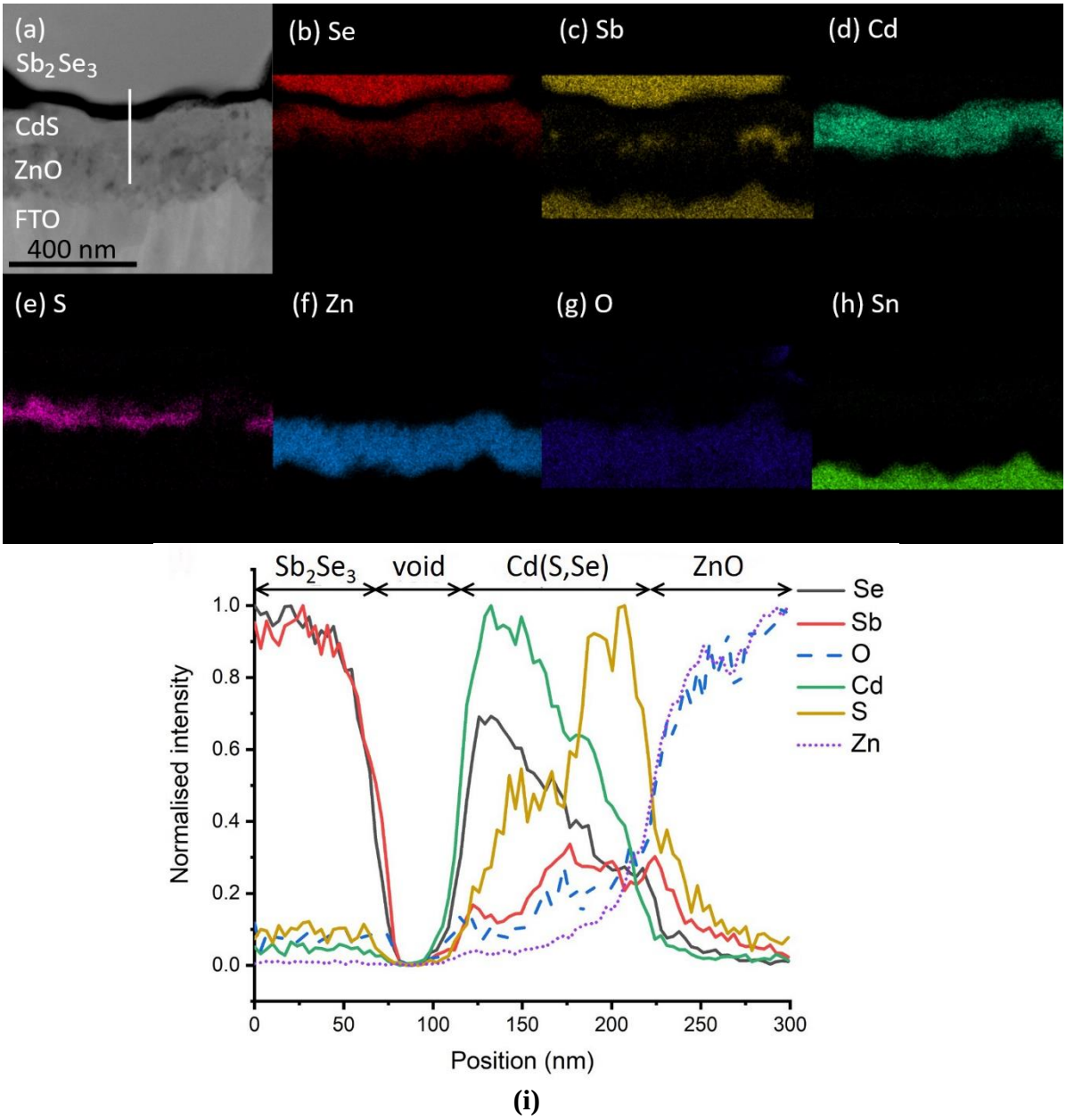

Figure 7. EDX chemical maps acquired across the Sb_2Se_3-CdS interface in the close space sublimated Sb_2Se_3-CdS sample. The STEM bright field image is shown in (a) with the individual layers labelled (FTO denotes fluorine doped SnO_2). EDX maps for Se, Sb, Cd, S, Zn, O and Sn are shown in (b)-(h) respectively. An EDX linescan was also acquired along the white line in (a) and plotted in (i) with the maximum EDX signal for each element normalized. The approximate regions of the different layers are indicated in (i), with Cd(S,Se) denoting the inter-diffused CdS layer.

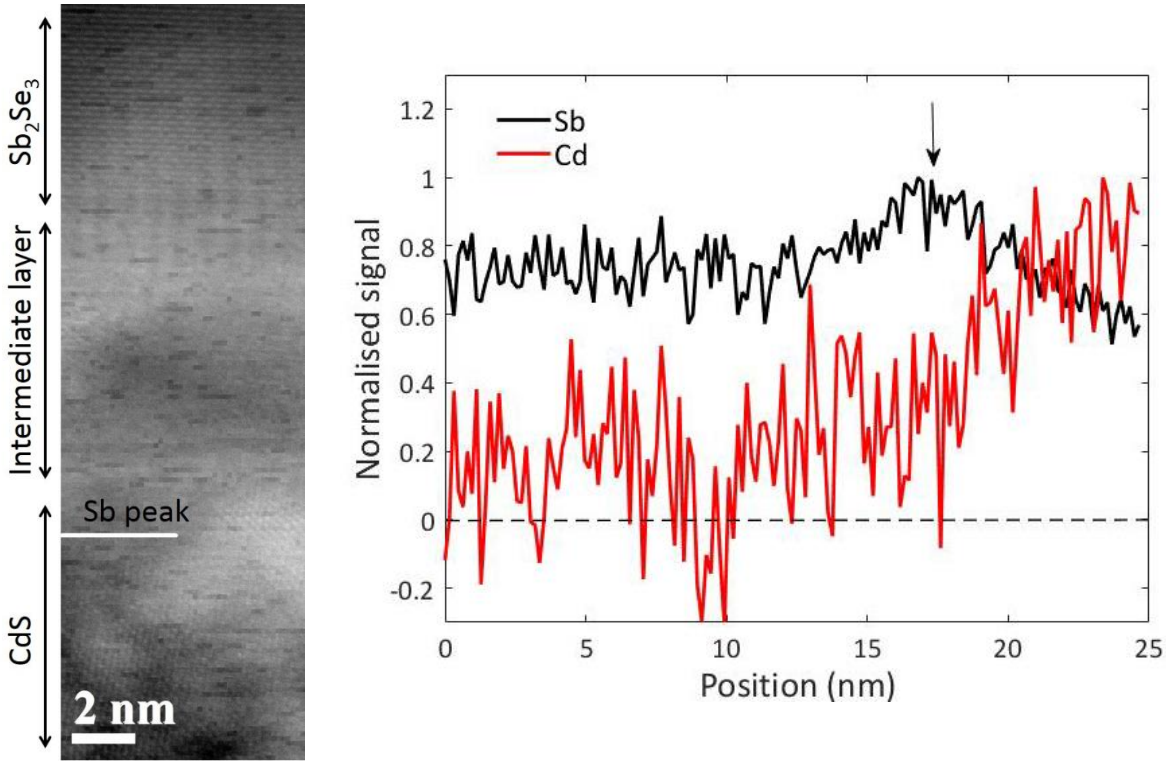

Figure 8. (a) MAADF image of the Sb_2Se_3-CdS interface in the thermal evaporated Sb_2Se_3-CdS device. The uneven intensity in the image is due to small fluctuations in the STEM probe current. (b) shows the EELS line profiles for Sb and Cd obtained from chemical maps of the same region as (a). When plotting (b) the EELS intensity was integrated in the horizontal direction, i.e. parallel to the Sb_2Se_3-CdS interface. The maximum EELS intensity for each element is normalized for a direct visual comparison. The location of the Sb peak intensity (vertical arrow in (b)) is indicated in (a).

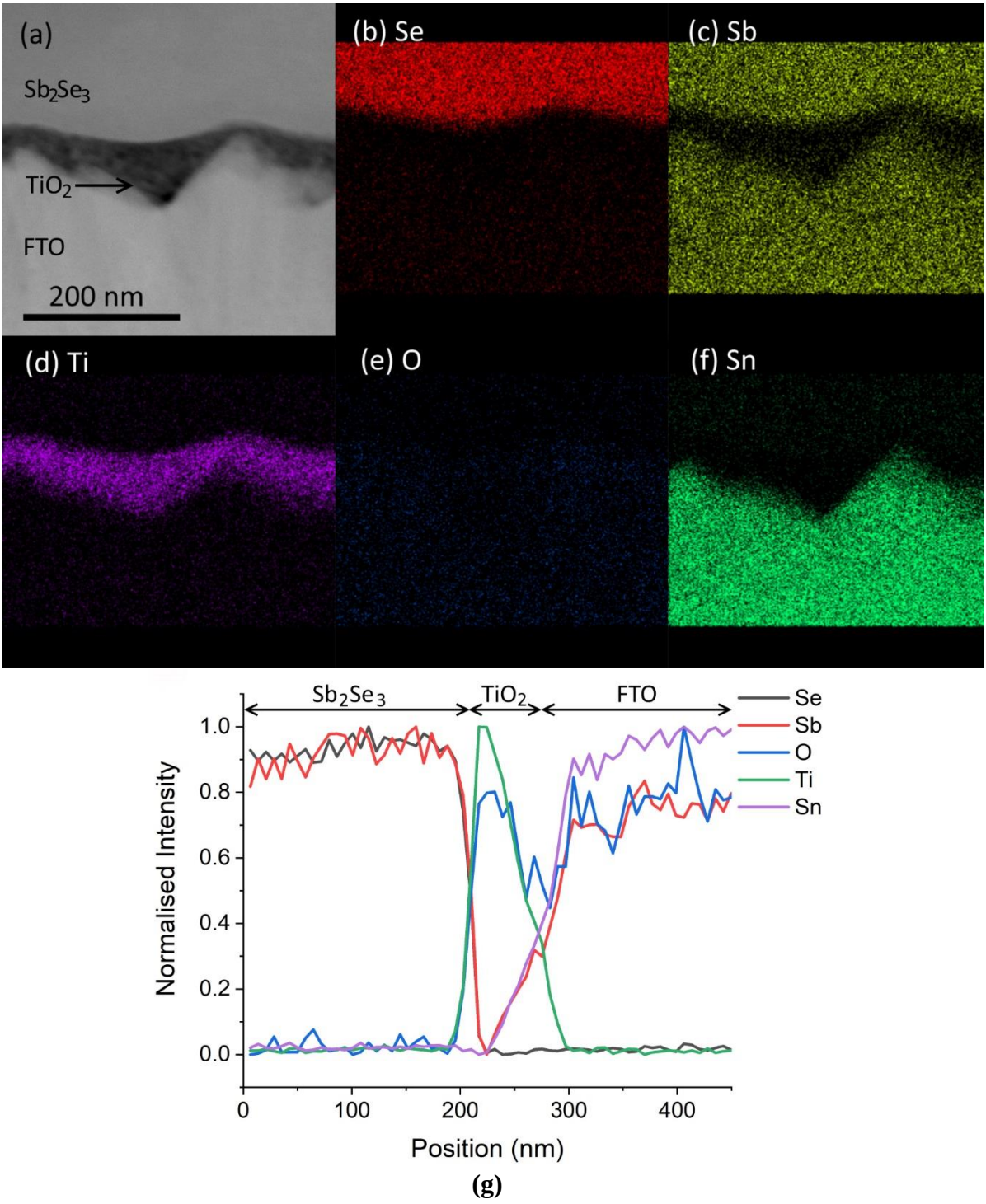

Figure 9. EDX chemical maps acquired across the Sb_2Se_3-TiO_2 interface in the close space sublimated Sb_2Se_3-TiO_2 sample. The STEM bright field image is shown in (a) with the individual layers labelled (FTO denotes fluorine doped SnO_2). EDX maps for Se, Sb, Ti, O and Sn are shown in (b)-(f) respectively. An EDX linescan from a different region is plotted

in (g) with the maximum EDX signal for each element normalized. The approximate regions of the different layers are indicated.

Table of Contents Graphic